JOURNAL OF PHARMA INSIGHTS AND RESEARCH ISSN NO. 3048-5428

REVIEW ARTICLE

Applications of Intradermal Optical Biosensing Tattoos in Real-Time Interstitial Fluid Biomarker Telemetry

Shaik Munnisha Begam*, Bhanusri Kadali, Bhavya Bhanu Botchu, Divya Mandru, Malleswari Peddiboina, Poornasri Varahagiri

Department of Pharmaceutical Analysis, KGRL College of Pharmacy, Bhimavaram, Andhra Pradesh, India

Publication history: Received on 27th May 2026; Revised on 2nd July 2026; Accepted on 4th July 2026

Article DOI: 10.69613/sbk9hq51

Abstract: Continuous tracking of physiological status demands diagnostic platforms capable of bridging high-fidelity biofluid interaction with non-obstructive signal transduction. Smart tattoo biosensors provide prolonged monitoring of interstitial fluid, which correlates robustly with systemic capillary blood levels for vital micromolecules by placing functional sensing formulations directly within the vascularized dermis. These platforms transform cutaneous tissue into an active analytical surface without rigid onboard power components, integrated silicon electronics, or transcutaneous physical penetrations during operation. Colorimetric and fluorometric transducer chemistries enable quantitative parameterization through either ambient light reflectance profiling or dedicated optoelectronic interrogation spanning visible and near-infrared optical windows. This manuscript consolidates the physiological foundations of intradermal biosensing, analytical ink architectures, matrix protection formulations, external optical readout interfaces, and systemic biological responses. Mass transfer limitations induced by post-implantation foreign body cascades, matrix optical clearing, *in vivo* fluorophore preservation, and enzymatic deactivation pathways receive critical evaluation. Current engineering techniques, such as zwitterionic hydrogel scaffolding, sacrificial co-enzymes, and supramolecular non-enzymatic affinity recognition schemes, present definitive routes toward operational baseline stability. The technological trajectory, clinical safety classification criteria, manufacturing consistency requirements, and ethical implications governing irreversible intradermal placement are delineated to chart the translation of dermal biosensors from proof-of-concept into verified diagnostic tools.

Keywords: Interstitial fluid biosensors; Intradermal nanoprobes; Dermal tattoo diagnostics; Near-infrared fluorescence; Optical biomarker telemetry.

1. Introduction

Continuous biomarker monitoring is vital for treating chronic conditions, tracking dynamic physiological conditions, and advancing decentralized precision medicine [1, 2]. Conventional tracking frameworks rely heavily on discrete capillary blood extraction [2, 3]. While analytical gold standards operate on blood samples, episodic vascular disruption induces progressive tissue trauma, increases risk of infection, and yields discontinuous snapshots that miss rapid glycemic fluctuations, transient lactacidemia, or sudden electrolyte perturbations [3, 4]. Continuous glucose monitors (CGMs) employing subcutaneously inserted needle-type electrochemical probes address sampling frequency deficits [5, 6]. However, transcutaneous configurations cause mechanical displacement, require repeated adhesive replacements, present chronic dermal irritation, and require discarded battery-driven transmitter units, impeding non-obstructive deployment [7, 8]. Cutaneous biosensing has expanded into non-invasive epiderma-interfaced sweat and interstitial fluid (ISF) analysis [9, 10]. Nevertheless, superficial epidermal sensors must overcome sweat gland stimulation variability, evaporative concentration shifts, fluidic sample collection delays, and physical detachment during rigorous physical motion [11, 12]. Intradermal smart tattoo biosensors circumvent superficial epidermal barriers by embedding bio-responsive functional ink matrices directly into the papillary and upper reticular dermis [13, 14]. In contrast to cosmetic pigments designed exclusively for structural persistence and optical opacity, these dynamic biosensing materials interface intimately with dermal interstitial fluid [14, 15]. Continuous plasma ultrafiltration creates dermal interstitial fluid that exhibits high stoichiometric parity with blood plasma regarding small molecular metabolites, peptides, and vital electrolytes [2, 16].

Combining active chromogenic dyes, near-infrared (NIR) fluorophores, supramolecular ionophores, or whole-cell genetic expression vectors into intradermal matrices converts the skin into a dynamic living display [14, 17]. These platforms operate without onboard lithium batteries, hardwiring, or subcutaneous mechanical anchors [1, 13]. Passive optical interrogation using ambient light or targeted optoelectronic platforms translates biochemical interactions within the interstitial fluid into optical signals [10, 18]. Realizing consistent *in vivo* tracking requires overcoming physiological defense mechanisms, optical attenuation, and chemical matrix attrition [19, 20].

* Corresponding author: Shaik Munnisha Begam

Figure 1. Comparison of cutaneous biosensing methods

Transcutaneous needles compromise epidermal integrity and rely on bulky physical anchors, while surface epidermal patches face external evaporative instability. Intradermal smart tattoo biosensors reside stably inside the skin for passive optical interrogation

Introducing functional particulate matrices into dermal tissue incites a protective foreign body response (FBR) [21, 22]. The ensuing inflammatory cascades, persistent macrophage fusion, and downstream collagenous fibrotic encapsulation impose substantial steric mass-transport diffusion barriers that compromise analytical temporal fidelity [22, 23]. Photobleaching from solar radiation, non-specific macromolecular protein adsorption, reactive oxygen species generation, and structural denaturation of proteinaceous biocatalysts limit operational sensor life [20, 24]. Resolving these biophysical and biochemical hurdles requires coordinating functional biomaterial matrices, protective nano-architectures, and optical calibration protocols [14, 25, 26]. This work outlines the core principles of intradermal sensing platforms, tracing metabolite transport across dermal microenvironments to responsive ink nanostructures, quantitative telemetry setups, and biomedical validation protocols [2, 13, 14, 27].

2. The Dermal Interstitial Fluid Compartment

2.1. Skin Anatomy

Deploying functional biosensor formulations into the cutaneous barrier requires strict spatial localization relative to skin histology [2, 28]. Human skin comprises three functional zones: the cellular, avascular epidermis; the vascularized, collagen-dense dermis; and the underlying adipose-rich hypodermis [28, 29]. The epidermis is capped externally by the stratum corneum, an anucleated, keratin-packed lipid matrix roughly 10 to 20 micrometers thick that limits outward water vapor loss and blocks external xenobiotic ingress [29, 30]. Underlying basal keratinocytes divide and migrate upward continuously, sloughing off during a 28-day turnover cycle [28]. Biorecognition inks deposited superficially within the epidermis will shed during regular cellular turnover [13, 14].

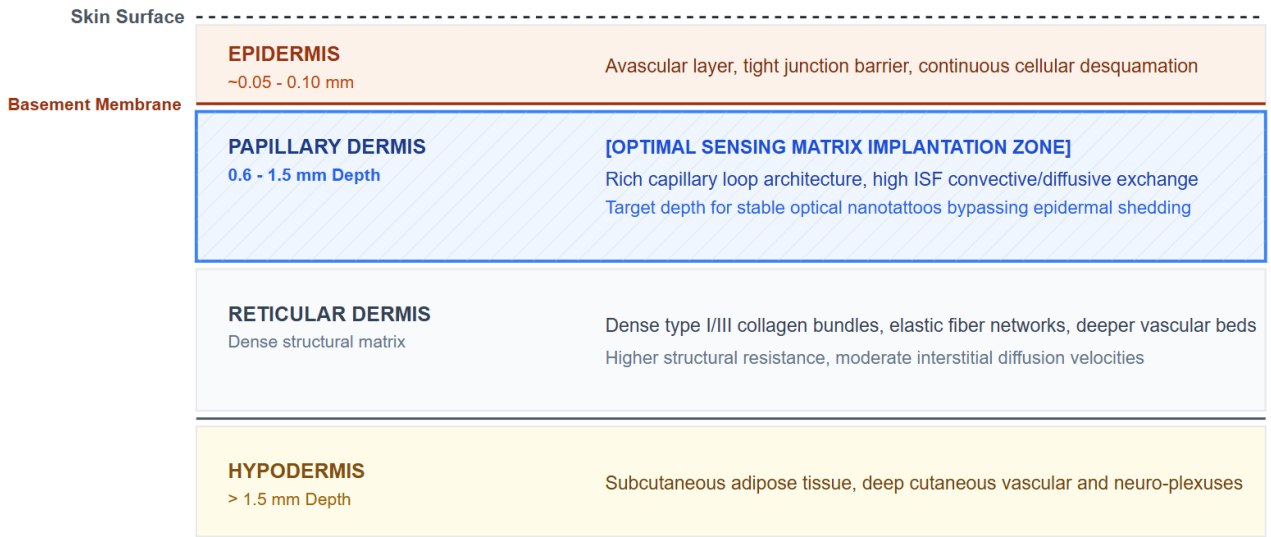

Figure 2. Anatomical localization and stratigraphic depth boundaries.

Dermal smart tattoos require strict spatial deposition into the vascularized papillary and reticular dermis (0.6–1.5 mm). Positioning at this depth avoids superficial cellular turnover while remaining within the rapid transvascular exchange zone of interstitial fluid.

Functional intradermal smart tattoos are localized beneath the basement membrane within the papillary and upper reticular dermis, spanning operational depths between 0.6 mm and 1.5 mm [14, 31]. The dermis bypasses cellular turnover cycles, consisting of an extracellular matrix (ECM) rich in type I and type III fibrillar collagen, elastic fibers, and an amorphous ground substance composed of glycosaminoglycans and proteoglycans [28, 32]. This structural composition preserves immobilized nano-architectures across extended monitoring windows [25, 33].

The dermal microcirculation is organized into interconnected vascular plexuses: a deep subpapillary plexus along the dermal-subcutaneous junction and a superficial plexus beneath the dermal papillae [28, 34]. Ascending arterioles feed terminal microvascular loops that reach the papillary pegs [34, 35]. These microvascular capillary loops deliver nutrients, regulate systemic thermal dissipation, and generate the dermal interstitial fluid microenvironment [2, 35].

2.2. Capillary Ultrafiltration of Interstitial Fluid

Dermal interstitial fluid functions as the immediate mass-exchange matrix separating cutaneous cells from circulating terminal blood vessels [2, 16]. Hydrophilic metabolites, mineral ions, and metabolic waste exchange across this fluid medium [16, 36]. The generation and directional turnover of interstitial fluid depend on transcapillary fluid motion, governed by Starling fluid equilibrium [2, 36]:

$$J_v = K_f[(P_c - P_i) - \sigma(\pi_c - \pi_i)]$$

Here, J_v denotes the net transvascular fluid filtration volume per unit surface area, K_f represents the hydraulic permeability coefficient of the capillary endothelium, and P_c and P_i denote capillary hydrostatic pressure and interstitial free fluid hydrostatic pressure, respectively [36]. The term σ reflects the osmotic reflection coefficient for macro-proteins, while π_c and π_i correspond to the colloid osmotic (oncotic) pressures of plasma and interstitial fluid [2, 36].

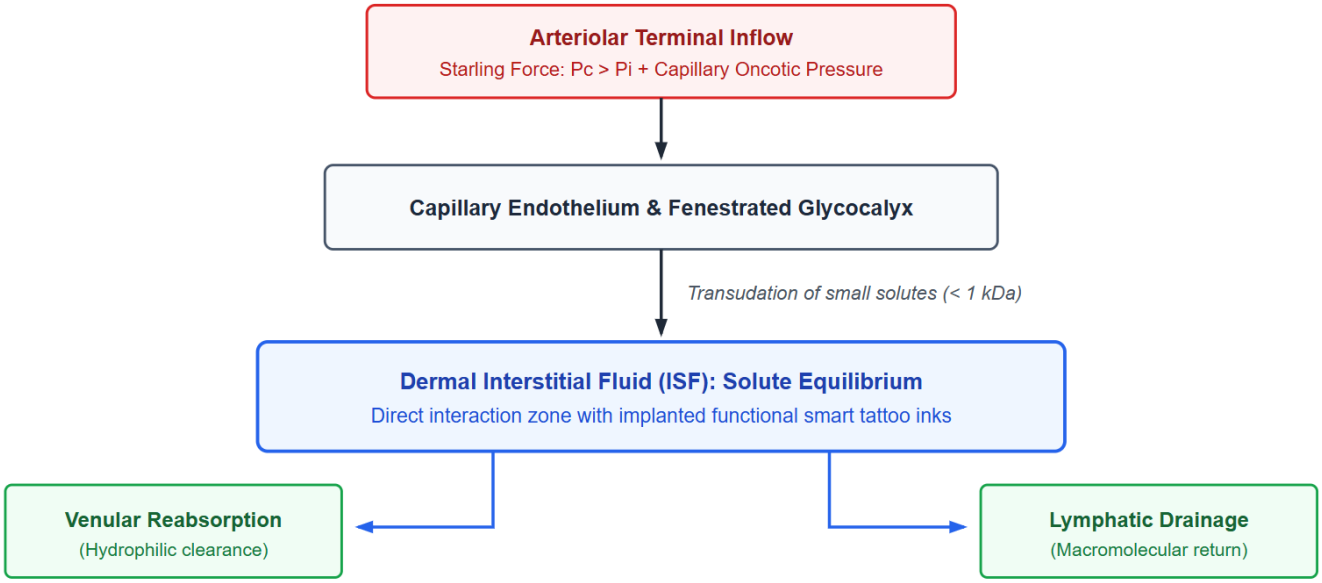

Figure 3. Interstitial Solute Exchange across Dermal Microcirculation

Under normal physiological hemodynamics, net filtration dominates the arteriolar terminus of the papillary loops, moving water, dissolved electrolytes, and low-molecular-weight molecules across the endothelial glycocalyx into the extracellular matrix [36, 37]. Much of this fluid returns directly to systemic circulation at the venular terminal plexus, with the remaining fraction entering initial blind-ended dermal lymphatic capillaries for downstream thoracic reinjection [37, 38]. This hydraulic cycling maintains steady convective and diffusive transport of plasma-derived constituents through the dermal interstitium [2, 16].

2.3. Blood-to-Interstitial Fluid Partitioning

Intradermal sensing matrices do not quantify blood components directly; they track target species concentrations within the surrounding interstitial fluid [2, 14]. Leveraging the dermal interstitial matrix for systemic monitoring requires understanding analyte partitioning and mass transport kinetics [2, 16]. Low-molecular-weight hydrophilic species (<1kDa), such as D- Glucose (180.6 Da),

L-lactate (89.07 Da) and small mono-and divalent electrolytes (Na^+, K^+, Cl^-), pass freely through capillary fenestrae and inter-endothelial clefts without steric restriction [2, 36]. Their partition coefficient between plasma and free interstitial water is effectively unity ($K_p \approx 1.0$) [2, 16].

Transport across the capillary wall into the dermal matrix proceeds primarily via passive diffusion along concentration gradients, modeled through Fick's first law [6, 39]:

$$J = -D_{\text{eff}} \frac{\partial C}{\partial x}$$

In this expression, J represents total solute flux, D_{eff} denotes the effective diffusion coefficient of the target analyte within the dense collagenous matrix, and $\partial C / \partial x$ corresponds to the local concentration gradient between the capillary endothelium and the sensing matrix [39]. The effective diffusion coefficient within the dermis is constrained by matrix tortuosity (τ) and steric hindrance (F_{steric}) relative to free aqueous environments (D_0) [23, 39]:

$$D_{\text{eff}} = D_0 \frac{F_{\text{steric}}}{\tau^2}$$

Macromolecular proteins, such as serum albumin (≈66.5 kDa) and immunoglobulins (≈150 kDa), display reflection coefficients approaching unity ($\sigma \to 1$), significantly limiting their baseline extravasation [2, 36]. Dermal interstitial fluid thus operates as a physiological ultrafiltrate of plasma [2, 16].

Because analyte transport depends on diffusion across the interstitial spatial gap separating dermal capillaries from the sensor surface, temporal lag periods emerge during rapid systemic concentration swings [6, 40]. *In vivo* physiological lag times typically range between 3 and 12 minutes for D-glucose, varying with cutaneous capillary perfusion, localized ambient temperature, hydration states, and the anatomical distance between functional tattoo aggregates and microvessels [6, 40]. Dynamic calibration algorithms must model this transport delay to preserve analytical correlation with instantaneous arterial and venous concentrations [6, 18].

3. Transduction and Responsive Biomaterial Inks

3.1. Colorimetric Transduction Systems

Colorimetric intradermal formulations convert analyte concentrations into visible spectral absorption shifts (λ=400 to 700 nm), enabling qualitative assessment or spectrophotometric quantification via ambient illumination without external electronic excitation [14, 18].

3.1.1. Enzymatic Formulations

Colorimetric enzymatic inks rely on coupled oxidoreductase-peroxidase biocatalysis [14, 41]. Tracking non-electroactive sugars like D-glucose or monocarboxylates like L-lactate typically involves co-immobilizing a primary flavoprotein oxidase with a reporter peroxidase and a chromogenic dye substrate within an intradermal hydrogel network [14, 42].

In glucose tracking, glucose oxidase (GOx, EC 1.1.3.4) oxidizes β-D-glucose to D-glucono-1,5-lactone, reducing its flavin adenine dinucleotide (FAD) cofactor to $FADH_2$ [41, 43]:

$$\beta\text{-D-Glucose} + \text{GOx(FAD)} \longrightarrow \text{D-Glucono-1,5-lactone} + \text{GOx}(FADH_2)$$

Dissolved interstitial molecular oxygen (O_2) re-oxidizes the enzyme back to its resting state, producing hydrogen peroxide (H_2O_2) [41, 43]:

$$\text{GOx}(FADH_2) + O_2 \longrightarrow \text{GOx(FAD)} + H_2O_2$$

A co-immobilized peroxidase, such as horseradish peroxidase (HRP, EC 1.11.1.7), then consumes the produced hydrogen peroxide to catalyze the single- or double-electron oxidation of a chromogenic electron donor [14, 43]:

$$H_2O_2 + DH_2 \xrightarrow{HRP} 2H_2O + D^*$$

Typical chromogens include 3,3',5,5' -tetramethylbenzidine (TMB), o -phenylenediamine (OPD), and 2,2' -azino-bis(3-ethylbenzothiazoline-6-sulfonic acid) (ABTS) [14, 44]. Oxidizing TMB drives successive single-electron charge-transfer complexes that shift solution absorption from transparent to blue (λ_{max}=652 nm), transitioning to a yellow diimine derivative (λ_{max}=450 nm) upon complete double oxidation under local acidic conditions [14, 44]. Table 1 summarizes the core operational principles, material matrices, readouts, and translational constraints across the primary intradermal optical transduction modalities.

Table 1. Comparative Evaluation of Intradermal Optical Transduction Modalities

Transduction Modality	Recognition & Transduction Mechanism	Matrix & Carrier Formulation	Optical Readout & Quantification	Major Advantages	Target Analytes
Colorimetric Enzymatic Cascade	Biocatalyzed substrate oxidation (GOx, LOx) coupled with peroxidase-driven chromogen dye oxidation (TMB, ABTS)	Poly(hydroxyethyl methacrylate) (pHEMA) or alginate hydrogels	Visible reflectance shifts ($\lambda =$ 400 to 700 nm) under ambient light or white LED	Zero-power requirement; immediate qualitative visual assessment via naked eye or smartphone	D-Glucose, L-Lactate, Uric acid
Ionophore-Based Bulk Optode	Reversible thermodynamic ion extraction coupled with deprotonation of a lipophilic chromoionophore	High-molecular-weight PVC / poly (decyl methacrylate) plasticized with DOS nanospheres	Visible-to-NIR absorption / fluorescence ratiometric shifts ($\lambda =$ 500 to 800 nm)	Fully reversible thermodynamic equilibrium; zero substrate consumption; high ionic selectivity	K^+, Na^+, Ca^{2+}, Cl^-, H^+ (pH)
Near-Infrared Fluorometric Probe	Analyte-induced Photoinduced Electron Transfer (PET) modulation or Förster Resonance Energy Transfer (FRET)	Core-shell mesoporous silica nanoparticles (MSNs) or polymeric nanocapsules	Emission intensity or lifetime shifts within NIR-I/II biological windows ($\lambda =$ 650 to 1350 nm)	Deep cutaneous photon penetration; complete elimination of melanin/hemoglobin optical distortion; invisible display	D-Glucose, Interstitial oxygen, Nitric oxide, Heavy metal ions
Engineered Whole-Cell Living Sensor	Biomarker binding to chimeric transcription factor driving de novo synthetic reporter protein expression	Tough, nanoporous alginate-polyacrylamide interpenetrating hydrogels	Bioluminescence or fluorescent protein emission (GFP, mCherry) ($\lambda =$ 480 to 610 nm)	Complex multi-analyte processing (AND, OR logic); autonomous synthesis of signal amplifiers	Inflammatory cytokines (TNF-α), Bacterial endotoxins, Environmental toxicants

Enzymatic colorimetric cascades encounter structural limitations *in vivo* [19, 20]. These systems consume local molecular oxygen and substrate during signal generation, creating local hypoxia and analyte depletion when mass-transfer rates lag behind biocatalytic turnover [6, 43]. Traditional chromophore oxidation forms covalent conjugated backbones, yielding irreversible color transformations unsuited for dynamic tracking [14, 44]. Reversible intradermal colorimetry requires reversible redox dyes, continuous substrate-product clearance, or non-destructive supramolecular equilibrium indicators [14, 45].

3.1.2. Supramolecular Ionophore and Chromoionophore Systems

Targeting non-redox physiological ions (H^+, Na^+, K^+, Ca^{2+}, Cl^-) demands reversible thermodynamic equilibrium rather than metabolic substrate consumption [14, 45]. Modern ion-selective optode tattoo formulations encapsulate ion-recognition components within lipophilic, plasticized polymeric nanospheres, commonly composed of high-molecular-weight poly(vinyl chloride) (PVC) or poly(decyl methacrylate) matrices [45, 46].

These optode nanospheres integrate three critical components [45, 46]:

1. A neutral, highly lipophilic synthetic ionophore (L) designed to selectively chelate the target ion via coordination complexes (e.g., valinomycin displaying an exceptionally high selectivity for K^+ over Na^+ of $\approx 10^4$) [46, 47].
2. A lipophilic chromoionophore (CH^+), which functions as a proton-sensitive dye possessing an engineered lipophilic side chain that prevents phase migration into the aqueous ISF [45, 48].
3. Lipophilic organic ionic sites (R^-), such as potassium tetrakis[3,5-bis(trifluoromethyl)phenyl]borate, that maintain continuous electrical electroneutrality within the organic nanoparticle domain [46, 48].

Thermodynamic ion exchange between the aqueous dermal interstitial fluid and the tattoo nanosphere drives the optical transduction process [45, 48]:

$$I^{z+}_{(\mathrm{ISF})} + z\,\mathrm{CH}^+_{(\mathrm{tattoo})} + L_{(\mathrm{tattoo})} \rightleftharpoons \quad K_{\mathrm{ex}} \quad IL^{z+}_{(\mathrm{tattoo})} + z\,\mathrm{C}_{(\mathrm{tattoo})} + z\,\mathrm{H}^+_{(\mathrm{ISF})}$$

When target interstitial cations (I^{z+}) partition across the nanosphere boundary and bind the neutral ionophore, electrical neutrality forces proton de-intercalation from the chromoionophore (CH^+) into the adjacent extracellular fluid [45, 48]. Deprotonating the chromoionophore changes its conjugated molecular architecture, driving a visible spectral absorption shift [45, 48]. Because this thermodynamic exchange is reversible, decreases in interstitial cation concentrations drive proton re-uptake and restore the resting spectrum [45]. However, because the system relies on co-extraction equilibrium, the local optical response depends on both target ion activity and local interstitial pH [45, 48]. Addressing this co-dependence requires incorporating an independent, static pH-referencing probe to decouple cross-sensitivity [14, 48].

3.2. Fluorescent Nanoprobes and Photophysical Modulation

Fluorescent intradermal biosensors provide higher analytical sensitivity, lower detection thresholds, and wider dynamic ranges than colorimetric systems [10, 13]. By decoupling excitation light from emitted radiative decay, these systems limit light-scattering interference from cutaneous structures [10, 49].

3.2.1. Near-Infrared Optical Windows and Tissue Scattering

Visible optical tracking ($\lambda = 400$ to 650 nm) inside cutaneous tissue faces severe optical attenuation [49, 50]. Broadband absorption from epidermal melanin, along with oxygenated and deoxygenated hemoglobin within the dermal capillary beds, creates significant signal loss [49, 50]. Dense, fibrillar type I collagen bundles and elastic fibers scatter visible light, causing photon paths to drift through Rayleigh and Mie regimes [50, 51]. These scattering dynamics distort excitation light and reduce optical telemetry accuracy [10, 51].

To optimize photonic transport, intradermal fluorophores are engineered to operate within the biological optical transparency windows [49, 52]:

- NIR-I Window: spans 650 nm to 950 nm, where hemoglobin and water absorption profiles reach local minima, limiting non-specific autofluorescence from dermal structural proteins (such as collagen crosslinks and elastin) [49, 52].
- NIR-II Window: spans 1000 nm to 1350 nm, where Mie scattering decreases dramatically ($\propto \lambda^{-\alpha}$, where $1 \leq \alpha \leq 4$), allowing photons to traverse several millimeters of dermal tissue with preserved spatial coherence and low background noise [52, 53].

3.2.2. Quenching Cascades and Energy Transfer Kinetics

Dynamic fluorescent tracking leverages specific physical quenching interactions between the fluorophore and target analyte [10, 54]. Photoinduced Electron Transfer (PET) systems separate a receptor unit possessing a high-energy non-bonding electron pair (such as an aliphatic tertiary amine) from the primary fluorophore via an insulating spacer [54, 55]. Under baseline states, light excitation excites electrons in the fluorophore, leaving an unfilled lower orbital that accepts an electron from the receptor's unshared lone pair [55]. This process quenches fluorescence via non-radiative decay [55]. When the target analyte coordinates with the receptor, the lone pair's oxidation potential shifts, blocking the PET pathway and restoring fluorescence emission [54, 55].

Förster Resonance Energy Transfer (FRET) architectures rely on non-radiative, dipole-dipole energy transfer over nanometer distances [10, 56]. The energy transfer efficiency (E) depends on the separation distance (r) between donor and acceptor fluorophores [56]:

$$E = \frac{R_0^6}{R_0^6 + r^6}$$

Here, R_0 denotes the Förster distance, where transfer efficiency equals 50% (typically 2 to 8 nm) [56]. Conformation-switching synthetic receptors or functional aptamers bring donor and acceptor fluorophores into proximity or push them apart upon analyte binding, modulating donor-to-acceptor emission ratios [56, 57]. This ratiometric shift provides an internal reference that resists variations in total excitation light intensity, absolute sensor concentration, and tissue movement [10, 57].

Nanomaterial-based platforms expand on these molecular systems [13, 58]. Single-walled carbon nanotubes (SWCNTs) wrapped in functional polymers yield stable NIR-II fluorescence emission that resists photobleaching, while semiconductor quantum dots (QDs) offer narrow, tunable emission spectra alongside broad optical absorption profiles [58, 59].

3.3. Synthetic Biology and Genetically Engineered Living Inks

A distinct approach to smart tattoo design integrates genetically modified microorganisms, such as *Saccharomyces cerevisiae* or *Escherichia coli*, encapsulated within semi-permeable intradermal hydrogels [17, 60]. These synthetic biology platforms use natural transcriptional networks to process complex biochemical inputs [60, 61].

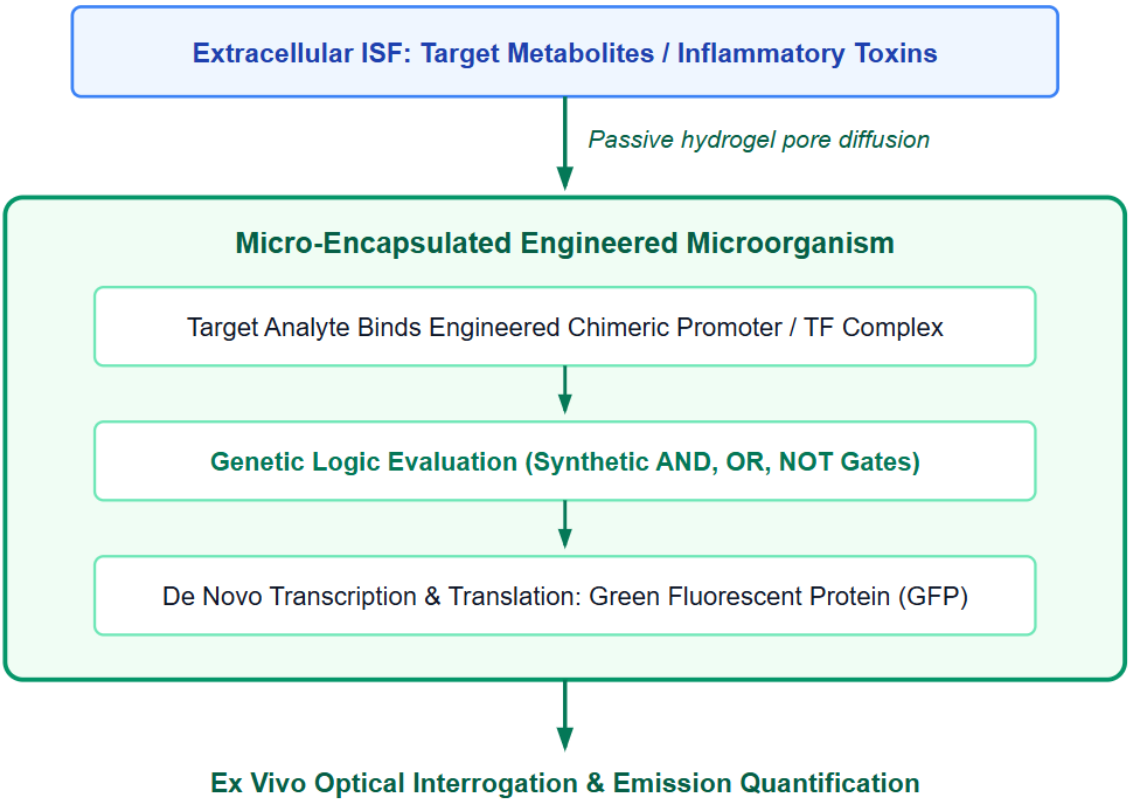

Figure 4. Intradermal synthetic biology sensing mechanism.
Genetically engineered bacteria or yeast inside nanoporous protective hydrogels run genetic logic circuits upon analyte binding, driving the synthesis of fluorescent proteins for non-invasive reading.

Engineered transcriptional factors link target recognition to reporter gene expression (such as Green Fluorescent Protein [GFP] or bacterial luciferase cascades) [60, 62]. Integrating synthetic biological logic gates (AND, OR, NOT) allows living biosensors to process multiple inflammatory cytokines or metabolic intermediates simultaneously, generating an optical readout only under specific pathological multi-marker signatures [60, 61].

These systems introduce specific biological containment and operational challenges [60, 63]. Encapsulating living cells within the dermis requires robust, nanoporous hydrogel architectures (e.g., tough alginate-polyacrylamide networks) that allow small-molecule nutrients and target analytes to enter while blocking outward microbial migration and host immune cell ingress [63, 64]. Maintaining

cell viability over extended timeframes requires continuous access to local ISF nutrients, and slow protein expression kinetics (ranging from 30 minutes to multiple hours) limits living inks to tracking long-term trends rather than immediate metabolic transients [17, 60].

4. Target Metabolites and Diagnostic Markers

Target metabolites within the dermal interstitial fluid serve as direct windows into systemic physiology [2, 16]. Interstitial fluid hosts diverse metabolic byproducts, critical electrolytes, and regulatory hormones that correlate with plasma profiles [2, 14].

Figure 5. Diagnostic biomarkers

Physiological targets within the dermal interstitial compartment, identifying corresponding clinical rationales and selective molecular transducer architectures

4.1. Primary Metabolic Intermediates: Glucose and Lactate

D-glucose monitoring remains the primary target for continuous biosensing platforms, driven by clinical demands for managing type 1 and type 2 diabetes mellitus [5, 6, 65]. Intradermal glucose levels reflect blood concentrations through rapid transcapillary transport, providing the temporal tracking needed to avoid severe hypoglycemia and chronic hyperglycemia [6, 66]. In non-enzymatic platforms, phenylboronic acid (PBA) derivatives serve as stable synthetic receptors, forming cyclic boronate esters with cis-1,2- or 1,3-diols on D-glucose molecules [67, 68]. Modulating boronic acid pK_a allows tuning binding affinities to match physiological interstitial glucose ranges (2 to 25 mM) without consuming local oxygen [68, 69].

L-lactate is an essential clinical metric for cellular hypoxia, exercise-induced anaerobic thresholds, tissue shock, and early-stage systemic sepsis [1, 70]. Under cellular oxygen deficits, pyruvate reduction yields elevated lactate concentrations that partition into the interstitial space [2, 70]. Intradermal tracking of lactate relies on lactate oxidase (LOx, EC 1.13.12.4), which selectively converts L-lactate to pyruvate and hydrogen peroxide, or recombinant bacterial cytochromes that undergo conformational changes upon substrate binding [42, 71]. Table 2 outlines the clinical targets validated for dermal interstitial fluid tracking, their optical transduction chemistries, and the physiological relevance of their dynamic detection ranges.

4.2. Homeostatic Electrolytes and Systemic Acid-Base Tracking

Monitoring systemic hydration, neuromuscular excitability, and renal ion retention relies on tracking mono- and divalent electrolytes [1, 2, 45]:

Sodium (Na^+) and Potassium (K^+): Intradermal sodium levels reflect systemic hypernatremia or hyponatremia, while potassium fluctuations directly alter cellular resting membrane potentials, where acute hyperkalemia creates risks for cardiac arrhythmia [2, 46]. Valinomycin-doped optode nanospheres allow precise optical potassium tracking down to narrow physiological shifts (3.5 to 5.2 mM) despite high background sodium concentrations [46, 47].

Table 2. Clinical Biomarker Matrix for Dermal Interstitial Fluid Telemetry

Target Biomarker	Physiological ISF Concentration Range	Molecular Mass (Da)	Transduction Chemistry & Responsive Ink Matrix	Interstitial-to-Blood Correlation & Latency	Clinical Diagnostic & Pathological Relevance
D-Glucose	2.0-25.0 mM (36-450 mg/dL)	180.16	Glucose oxidase (GOx) coupled with HRP/TMB, or synthetic phenylboronic acid (PBA) conjugates	$R > 0.92$; $5 - 12$ minute physiological lag under dynamic systemic shifts	Continuous glycemic profiling, type 1 and 2 diabetes management, avoidance of acute hypoglycemia
L-Lactate	$0.5 - 20.0$ mM	89.07	Lactate oxidase (LOx) with chromogenic electron acceptors or cytochrome b_2 binding domains	$R \approx 0.88$; $4 - 8$ minute transport delay from capillary bed	Cellular hypoxia, early sepsis stratification, physical exertion thresholds, circulatory shock
Potassium (K^+)	$3.5 - 5.5$ mM	39.10	Valinomycin-doped plasticized nanospheres with Chromoionophore I and lipophilic borate salts	$R \approx 0.95$; near-instantaneous local thermodynamic equilibrium ($<$ 3 minutes)	Hyperkalemia / hypokalemia screening, cardiac arrhythmia risk, acute renal dysfunction
Sodium (Na^+)	$135 - 145$ mM	22.99	Sodium ionophore X or 4-tert-butylcalix[4]arene-tetraacetic acid tetraethyl ester optodes	$R > 0.90$; rapid dynamic equilibration ($<$ 3 minutes)	Systemic hydration status, hypovolemia, electrolyte exhaustion during strenuous athletic exertion
Hydronium (pH)	$7.35 - 7.45$ (pathological: $6.8 - 7.8$)	1.01	Phenol red, bromothymol blue, or fluorescein isothiocyanate (FITC) covalently linked to hydrogels	Direct local microenvironment indicator; immediate equilibrium	Local tissue ischemia, metabolic acidosis, necrotizing tissue infection, skin barrier integrity
Uric Acid	$0.15 - 0.50$ mM	168.11	Urate oxidase (uricase) oxidation cascade or synthetic molecularly imprinted polymers (MIPs)	$R \approx 0.85$; $8 - 15$ minute equilibrium delay	Purine metabolism disorders, clinical gout monitoring, preeclampsia tracking, renal filtration decline

Cutaneous pH: Tracks localized metabolic acidosis, impaired wound healing, microvascular ischemia, and systemic acid-base shifts [2, 72]. Optical indicators like bromothymol blue, phenol red derivatives, or fluorescein isothiocyanate (FITC) conjugate into hydrogel networks to track physiological interstitial pH shifts between 7.35 and 7.45 [14, 72]. Local acidosis (pH < 7.30) shifts indicator deprotonation equilibrium, altering absorption spectra [14, 73].

4.3. Advanced Systemic Biomarkers: Uric Acid and Albumin

Beyond small primary metabolites, dermal interstitial fluid contains advanced diagnostic targets [2, 16]:

Uric Acid: Serves as the primary end product of purine catabolism in humans [2, 74]. Hyperuricemia reflects renal clearance deficits and indicates increased risk for gout, metabolic syndrome, and cardiovascular disease [74, 75]. Intradermal urate tracking uses urate oxidase (uricase, EC 1.7.3.3), which converts uric acid to 5-hydroxyisourate and hydrogen peroxide, or synthetic molecularly imprinted polymers (MIPs) engineered with sub-nanometer recognition pockets [75, 76].

Interstitial Serum Albumin: While normal transvascular reflection coefficients keep albumin concentrations lower in interstitial fluid than in plasma (≈ 15 to 20 g/L versus ≈ 35 to 50 g/L), albumin levels shift during systemic vascular leakage, severe systemic

inflammation, and localized microvascular damage [2, 36]. Tracking interstitial albumin uses lipophilic solvatochromic fluorophores or bromocresol green dye complexes embedded within high-porosity matrix hydrogels [14, 77].

5. *In Vivo* Degradation and Biocompatibility

Deploying biosensing formulations into the living dermis bypasses the stratum corneum, exposing synthetic materials to the host immune system [21, 22]. Translating these systems requires managing the foreign body response (FBR), enzymatic inactivation, and dye degradation within cutaneous tissue [22, 23].

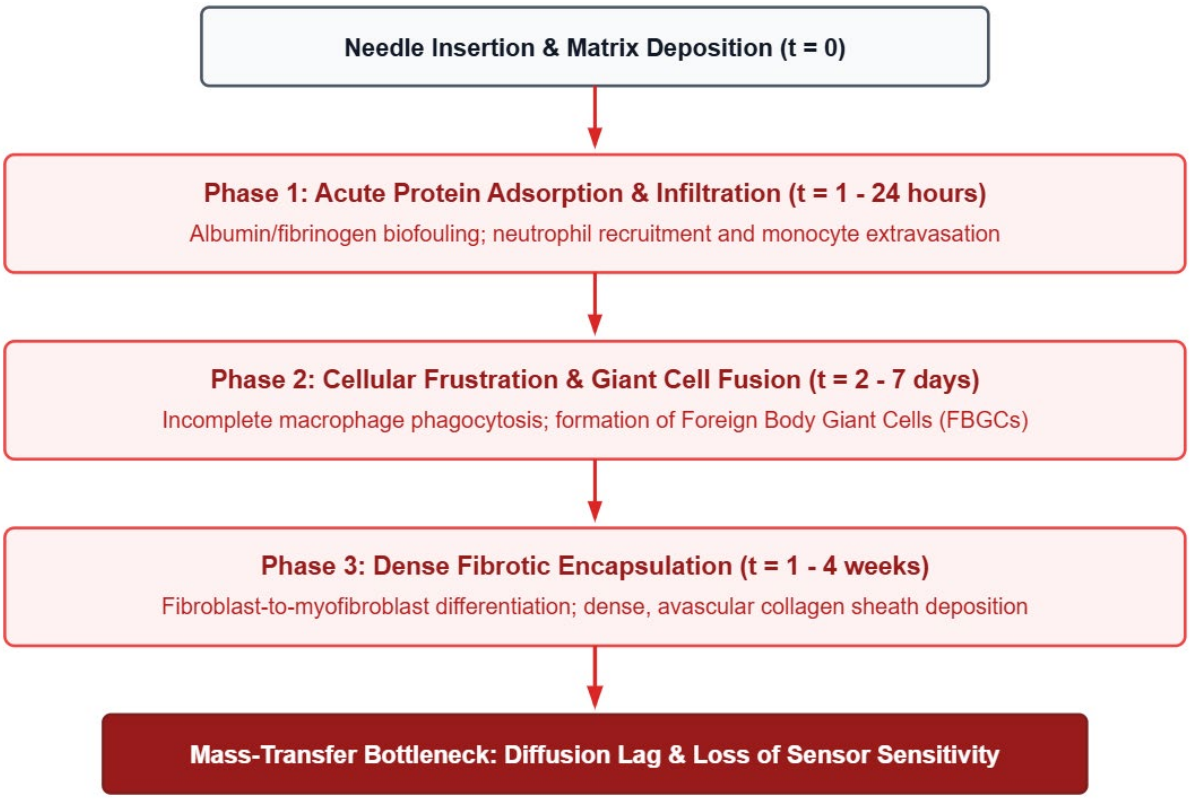

Figure 6. Progression of the Dermal Foreign Body Response (FBR)

5.1. The Dermal Foreign Body Cascade

Depositing smart inks into the vascularized dermis initiates a multi-phase foreign body cascade [21, 22]:

5.1.1. Phase 1: Acute Protein Adsorption and Early Inflammation

Mechanical penetration by solid or micro-needle injection disrupts capillary walls, releasing platelets, plasma fibrinogen, fibronectin, and vitronectin into the interstitial fluid [21, 22]. Within milliseconds, these proteins non-specifically adsorb onto the surface of the sensing nanoparticles or hydrogel networks [22, 78]. This adsorbed protein layer alters surface properties and guides the adhesion and activation of polymorphonuclear neutrophils, which migrate to the injection site within hours [22, 79]. Neutrophils release proteolytic enzymes and generate localized reactive oxygen species (ROS) via respiratory burst pathways [79, 80].

5.1.2. Phase 2: Cellular Frustration and Macrophage Fusion

Within 24 to 48 hours, systemic monocytes extravasate into the dermal space and differentiate into mature macrophages [21, 22]. Macrophages attempt to phagocytose the tattoo particles [14, 22]. If individual nanoparticles or crosslinked hydrogel aggregates exceed the critical phagocytic size limit (typically > 0.5 to $1.0\ \mu$m), macrophages encounter "frustrated phagocytosis" [21, 22]. Unable to engulf the larger structures, adjacent macrophages fuse their cell membranes to form multinucleated Foreign Body Giant

Cells (FBGCs) [22, 81]. These giant cells adhere to the sensor surface and secrete degradative lysosomal enzymes, hydrogen peroxide, and peroxynitrite radicals directly at the material interface [80, 81].

5.1.3. Phase 3: Dense Fibrotic Sheath Encapsulation

Sustained activation of FBGCs and tissue macrophages drives continuous paracrine secretion of pro-fibrotic cytokines, primarily Transforming Growth Factor-beta (TGF-β) and Platelet-Derived Growth Factor (PDGF) [22, 82]. These signals recruit local resting dermal fibroblasts and drive their differentiation into contractile myofibroblasts [82, 83]. Over several weeks, myofibroblasts deposit a dense, highly crosslinked collagenous capsule around the sensing matrix, composed of compact type I collagen bundles devoid of microvascular capillaries [22, 83]. Table 3 shows the physical and chemical degradation mechanisms active in the dermal microenvironment and maps them to target biomaterial mitigation strategies.

Table 3. Dermal Microenvironmental Degradation Pathways and Biomaterial Mitigation Strategies

Host Degradation Pathway	**Primary Biological or Chemical Effector**	***In Vivo* Failure Mechanism**	**Biomaterial Countermeasure**	**Mechanism of Action & Preservation Pathway**
Non-Specific Protein Adsorption	Circulating vitronectin, fibronectin, and plasma fibrinogen	Early protein biofouling triggers adhesion and activation of polymorphonuclear neutrophils	Zwitterionic polymer coronas (pCBMA , pSBMA)	Forms a tightly anchored, electrostatically driven hydration shell that renders biofouling thermodynamically unfavorable
Fibrotic Capsule Barrier	Multinucleated FBGCs and myofibroblast collagen secretion	Avascular type I collagen sheath restricts target solute diffusion, causing severe signal lag or loss	Controlled-release pro-angiogenic scaffolding (VEGF , bFGF)	Promotes capillary sprout invasion directly into the porous periphery, eliminating the avascular transport gap
Oxidative Degradation	Macrophage-derived ROS and reaction-generated H_2O_2	Radical-mediated cleavage of conjugated double bonds in chromophores, accelerating photobleaching	Co-immobilization of sacrificial Catalase	Catalyzes rapid disproportionation of H_2O_2 into H_2O and O_2, limiting self-inactivation
Proteolytic Denaturation	Matrix metalloproteinases (MMPs) and tissue proteases	Hydrolysis of peptide bonds unravels enzyme secondary and tertiary biocatalytic conformations	Mesoporous silica nanoparticle (MSN) encapsulation	Rigid, sub-nanometer pore networks ($2-4$ nm) allow small substrates to pass while excluding large proteases
Particulate Extravasation	Microvascular shear flow and initial dermal lymphatic drainage	Leaching of non-crosslinked fluorophores or nanoparticles < 10 nm, causing signal decay	Tailored covalent network crosslinking (pHEMA / EGDMA)	Controls average hydrogel mesh size ($\xi < 2$ nm) to physically trap sensor components while permitting analyte flux

This fibrotic capsule acts as a steric diffusion barrier that restricts mass transport of target analytes from adjacent functional capillaries to the tattoo biosensor [23, 84]. Dense collagen capsulation reduces effective diffusion coefficients (D_{eff}) by orders of magnitude, increasing sensor lag time from minutes to hours or causing complete signal attenuation [6, 23].

5.2. *In Vivo* Chemical Degradation

Beyond cellular encapsulation, the dermal microenvironment degrades sensor chemistries through distinct physical and chemical mechanisms [19, 20]:

- Enzymatic Denaturation: Bio-catalytic enzymes like glucose oxidase and lactate oxidase are optimized for specific physiological states [5, 41]. Prolonged exposure to dermal proteases, matrix metalloproteinases, and physiological temperatures ($37°$C) disrupts tertiary protein structures [20, 85]. This structural unfolding degrades catalytic activity over weeks *in vivo* [6, 85].

- Oxidative Stress and Photobleaching: Macrophage-derived reactive oxygen species combined with the continuous enzymatic generation of hydrogen peroxide in oxidoreductase cascades oxidize fluorophores and chromogenic dyes [20, 80]. Free radical oxidation cleaves conjugated double-bond networks, accelerating photobleaching and destabilizing baseline optical measurements [14, 86].
- Particulate Leaching and Systemic Clearance: Tattoo formulations composed of small molecules, linear polymers, or individual nanospheres smaller than roughly 10 to 20 nm gradually leak into initial dermal lymphatic vessels or cross fenestrated venules [21, 87]. This particulate leaching depletes active sensing components and introduces potential systemic clearance concerns [87, 88].

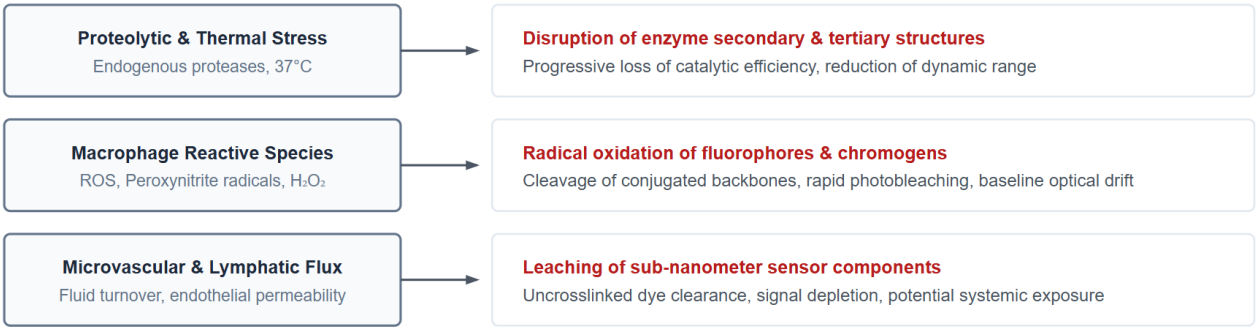

Figure 7. Mechanisms *In Vivo* Chemical and Physical Degradation

5.3. Biocompatibility Engineering Strategies

Overcoming the foreign body response and sensor degradation requires proactive biomaterials design [23, 25]:

5.3.1. Zwitterionic Hydrogel Networks

Coating or crosslinking biosensing inks with zwitterionic polymers such as poly(carboxybetaine methacrylate) (pCBMA) or poly(sulfobetaine methacrylate) (pSBMA) limits initial non-specific protein adsorption [25, 89]. Zwitterionic polymers maintain equal balances of anionic and cationic functional groups on each monomer unit [89, 90]. This charge distribution forms a tightly bound, structured hydration shell through electrostatic interactions, mimicking hydration layers found on zwitterionic cell membranes [90, 91]. Because removing water from this protective layer is thermodynamically unfavorable, circulating plasma proteins cannot directly contact the synthetic substrate [89, 91]. Preventing protein adsorption limits early neutrophil adhesion and circumvents downstream foreign body cascades, minimizing collagen encapsulation [23, 25].

5.3.2. Pro-Angiogenic Scaffolding

To eliminate the avascular void caused by fibrotic capsules, hydrogel matrices can incorporate controlled-release pro-angiogenic factors, such as recombinant human Vascular Endothelial Growth Factor (VEGF) or basic Fibroblast Growth Factor (bFGF) [23, 92]. Controlled delivery of these signaling proteins binds receptors on adjacent endothelial cells, promoting capillary sprout migration directly toward and through the outer porous boundary of the biosensing hydrogel [92, 93]. Maintaining a microvascular network near the active sensing domain shortens diffusion pathways, minimizes response lag, and maintains high correlation with systemic blood concentrations [2, 23].

5.3.3. Sacrificial Protective Co-Enzymes

To protect both the host tissue and co-immobilized sensing oxidases from locally generated hydrogen peroxide, formulations can co-encapsulate sacrificial enzymes like catalase (EC 1.11.1.6) [14, 94]. Catalase breaks down excess hydrogen peroxide into water and molecular oxygen [94]:

$$2\,H_2O_2 \xrightarrow{\text{Catalase}} 2\,H_2O + O_2$$

This degradation cascade prevents H_2O_2-induced oxidative crosslinking, limits local cytotoxicity, and replenishes molecular oxygen levels within the hydrogel to support continuous oxidase reactions [94, 95].

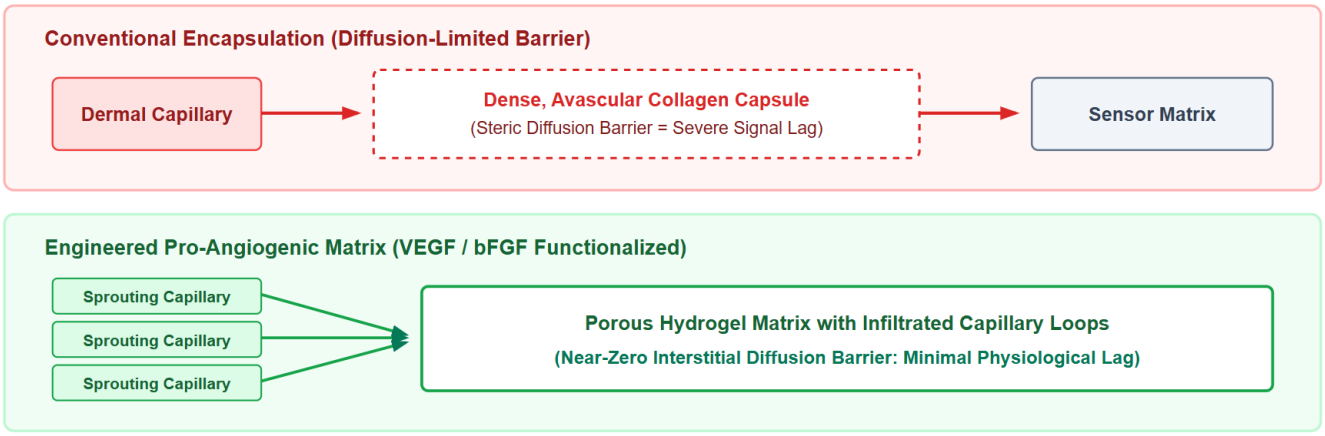

Figure 8. Comparison of Standard Fibrotic Sheath versus Pro-Angiogenic Scaffolding

5.3.4. Mesoporous Inorganic Nanoshields

Encapsulating organic fluorophores within mesoporous silica nanoparticles (MSNs) provides structural and optical protection [26, 96]. These silica networks feature ordered, tunable pore geometries (2 to 4 nm) that allow small targets (like D-glucose and mineral ions) to diffuse freely into the internal matrix while excluding larger host proteases, nucleases, and immunoglobulins [96, 97]. In addition, the rigid inorganic shell stabilizes encapsulated fluorophores against mechanical degradation and structural photolytic collapse [26, 98].

6. Design and Synthesis Methods

Formulating intradermal smart inks requires coordinating optical elements, synthetic scaffolds, and biological interfaces [14, 25, 33]. High-performance biosensing inks combine four functional layers:

1. Core Transduction Elements: Conjugated organic chromophores, fluorophores, quantum dots, or single-walled carbon nanotubes that modulate light absorption, emission intensity, or fluorescence lifetime [10, 58].
2. Biorecognition Receptors: Catalytic enzymes, synthetic boronic acid variants, ion-selective crown ethers, or immobilized aptamers that confer target selectivity [14, 68].
3. Protective Structural Scaffolds: Porous hydrogel networks, mesoporous silica spheres, or polymeric nanocapsules that contain functional components and regulate mass diffusion [25, 96].
4. Surface Biocompatibility Coronas: Exterior hydrophilic or zwitterionic polymer brush coatings designed to limit non-specific protein adsorption and suppress cellular foreign body cascades [25, 89].

6.1. Fabrication of Nanoporous Hydrogels

Immobilizing functional recognition chemistries inside the dermis typically uses synthetic or natural hydrogels that mimic native extracellular ground substances [25, 33]. Poly(2-hydroxyethyl methacrylate) (pHEMA) hydrogels provide stable mechanical platforms for smart tattoo applications [14, 33].

Crosslinked hydrogel networks are synthesized by free-radical solution polymerization of purified 2-hydroxyethyl methacrylate (HEMA) monomers alongside a bifunctional crosslinking agent, commonly ethylene glycol dimethacrylate (EGDMA, 0.5 to 2.0 mol%) [33, 99]. Polymerization is initiated using a thermal initiator like azobisisobutyronitrile (AIBN) or a redox system comprising ammonium persulfate (APS) and tetramethylethylenediamine (TEMED) [99]. Polymerizing these networks around pre-functionalized recognition nanoparticles produces a hydrophilic porous network [25, 99]. The average mesh size (ξ) is controlled by adjusting the molar crosslinking density (ρ_x) [39, 99]:

$$\xi = v_{2,s}^{-1/3} \left(\frac{2C_n \overline{M}_c}{M_r} \right)^{1/2} l$$

Here, $v_{2,s}$ represents the polymer volume fraction in the swollen state, $\overline{M}_c$ denotes the average molecular weight between adjacent crosslinks, M_r is the molecular weight of the repeating monomer unit, C_n represents the characteristic Flory ratio, and l corresponds to the carbon-carbon bond length [99]. By controlling the crosslinking density, the structural pore network can be engineered to allow target analytes like D-glucose (180 Da) to pass freely while physically trapping primary oxidase enzymes (≈ 160 kDa) and preventing macromolecular leaching into lymphatic vessels [14, 25].

6.2. Nano-Optode Architectures

Formulating lipophilic ion-selective tattoo nanospheres begins with dissolving high-molecular-weight poly(vinyl chloride) (PVC, ≈ 30 to 33 wt%) and an organic plasticizer, such as bis(2-ethylhexyl) sebacate (DOS, ≈ 60 to 66 wt%) in a volatile organic solvent (such as tetrahydrofuran, THF) [45, 46]. The plasticizer lowers the polymer's glass transition temperature (T_g) below body temperature (37°C), producing a flexible, hydrophobic fluid-like interior within the nanospheres [46, 100].

The target-selective ionophore (e.g., potassium-selective valinomycin), lipophilic chromoionophore (e.g., Chromoionophore I), and lipophilic borate salt additives are dissolved directly into this organic phase [45, 46]. This homogeneous solution is introduced dropwise into an aqueous surfactant solution (such as poly(ethylene glycol)-block-poly(propylene glycol)-block-poly(ethylene glycol), Pluronic F-127) under sonication [45, 100].

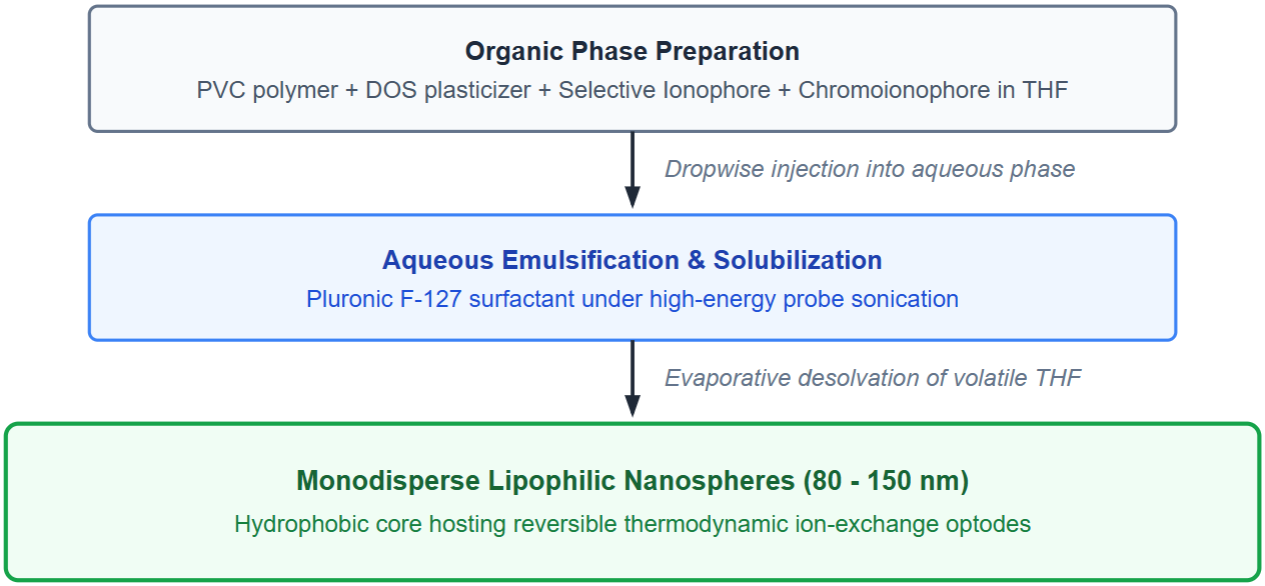

Figure 9. Self-Assembly of Ion-Selective Bulk Optode Nanospheres

Rapid evaporation of volatile solvent triggers self-assembly, yielding monodisperse polymeric nanospheres with average hydrodynamic diameters between 80 and 150 nanometers [45, 100]. These nanoscale structures maintain high surface-area-to-volume ratios that facilitate rapid ion exchange across the water-polymer interface, achieving sub-second optical response kinetics to local electrolyte shifts [45, 46].

7. System Interfacing, Optical Telemetry, and Quantitative Analytical Calibration

Intradermal smart tattoo biosensors function without internal silicon microchips, physical gold wiring, or onboard batteries [1, 13, 14]. Capturing diagnostic data requires external optical telemetry devices that illuminate the skin, collect reflected or emitted photons, and translate raw spectral data into calibrated clinical concentrations [10, 14, 18].

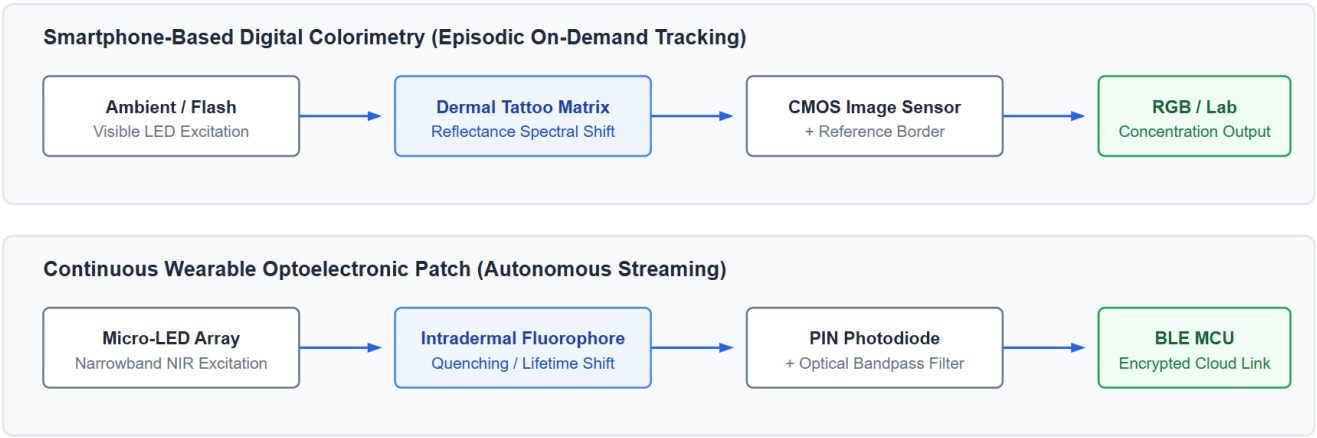

Figure 10. Optical Telemetry and Quantitative Estimation

7.1. Smartphone-Based Consumer Interfaces

Consumer smartphones provide optical readout platforms using integrated complementary metal-oxide-semiconductor (CMOS) camera sensors and white light-emitting diode (LED) sources [14, 18].

In a typical colorimetric workflow, the user photographs the dermal tattoo site [14, 18]. Computer vision software normalizes variations in ambient illumination and distance using an inert reference border printed around or micro-injected beside the active sensing zone [14, 101]. The software isolates the active sensing area and calculates coordinates across analytical color spaces [14, 101]:

- Red-Green-Blue (RGB): raw optical channel intensity mapping [18, 101].
- CIE $L^*a^*b^*$: device-independent color representation, where L^* tracks perceptual lightness, a^* represents the green-to-red axis, and b^* denotes the blue-to-yellow axis [14, 101].

Converting these color-space coordinates into target metabolite concentrations relies on calibration equations, such as Hill equations or polynomial regressions, derived during prior *in vitro* characterization [14, 45].

Smartphone-based colorimetry encounters challenges with variations in epidermal pigmentation [14, 50]. Cutaneous melanin absorbs broadly across the visible spectrum (400 to 700 nm), acting as a non-linear neutral-density optical filter that alters reflected light based on individual skin tone [50, 102]. Addressing this requires chromatic calibration algorithms that use the static reference ring to calculate the epidermal transfer function, mathematically removing melanin background absorption from the raw optical signal [14, 102].

7.2. Continuous Optoelectronic Wearable Patches

For autonomous, continuous data acquisition that bypasses manual smartphone scanning, miniaturized optoelectronic patches can be worn directly over the dermal tattoo [1, 10]. These flexible systems integrate surface-mount technology (SMT) on thin polyimide substrates, featuring [10, 103]:

- Narrowband micro-LEDs matched to the absorption maxima of the intradermal fluorophores [10, 52].
- Silicon PIN photodiodes capped with thin optical bandpass filters to isolate emitted fluorescence while blocking excitation light and ambient noise [10, 103].
- Low-power microcontrollers and Bluetooth Low Energy (BLE) antennas to transmit continuous telemetry streams to mobile devices or secure cloud databases [1, 103].

Operating in the near-infrared spectrum allows wearable optoelectronic patches to transmit excitation light through millimeters of cutaneous tissue, monitoring deep dermal fluorescence with minimal loss from epidermal pigmentation [49, 52, 103]. Table 4 lists out the architectural differences, optoelectronic specifications, processing requirements, and usage models between consumer smartphone-based readout systems and wearable patches.

Table 4. Technical Comparison of External Optical Telemetry Platforms

Technical Specification / Parameter	Smartphone Spectrophotometric Interface	Wearable Flexible Optoelectronic Patch
Excitation Illumination Source	Ambient natural/room light or phone white LED flash ($\lambda = 400 - 700$ nm)	Integrated surface-mount micro-LEDs (Narrowband visible or NIR: $650 - 1350$ nm)
Photonic Sensor Element	Built-in consumer CMOS image sensor array	Silicon PIN photodiodes capped with thin-film optical interference bandpass filters
Epidermal Melanin Filtering	Algorithmic chromatic correction based on static, unreactive reference borders	Deep-tissue near-infrared biological window illumination bypassing melanin attenuation
Data Acquisition Continuity	Intermittent / On-demand episodic photo capture (manual scanning required)	Autonomous, continuous real-time data streaming (adjustable sampling rates: $1 - 60$ Hz)
Primary Analytical Color Space	RGB, CIE $L^*a^*b^*$, or CIE XYZ chromatic coordinates	Ratiometric emission intensity or phase-resolved fluorescence lifetime decay
Power Infrastructure	Host smartphone rechargeable battery (zero wearable power footprint)	Miniaturized flexible lithium-polymer battery or wireless inductive NFC power harvesting
Data Transmission Interface	Direct on-device software calculation via localized computer vision	Bluetooth Low Energy (BLE) or NFC link to mobile device and cloud platforms
Target Clinical Context	Decentralized, routine chronic health monitoring and episodic screening	Critical care, dynamic athletic performance tracking, and continuous nocturnal diabetes care

8. Bottlenecks for Upscaling

Moving intradermal smart biosensors from animal models to human diagnostics introduces distinct regulatory, manufacturing, and bioethical considerations [2, 6, 21].

8.1. Regulatory Classification and Manufacturing Standards

Because intradermal smart tattoos monitor physiological biomarkers to guide medical decisions such as calculating insulin dosages regulatory bodies like the United States Food and Drug Administration (FDA) classify these systems as Class II or Class III medical devices [6, 104]. Unlike topical cosmetics or superficial patches, smart inks are deposited beneath the protective stratum corneum, requiring evaluation under medical device standards [104, 105]. Formulations must meet ISO 10993 standards for medical device biocompatibility, requiring testing for cytotoxicity, intracutaneous reactivity, subchronic systemic toxicity, genotoxicity, and carcinogenicity [21, 105].

Transitioning to commercial medical production requires strict Good Manufacturing Practices (GMP) [6, 104]. Traditional decorative tattoo pigments are manufactured without precise compositional controls, often exhibiting batch-to-batch variations in heavy metal impurities and broad particle size distributions [14, 106]. In contrast, diagnostic dermal inks demand tight synthesis specifications [6, 104]:

- Chemical Purity: $> 99.9\%$ trace metal analysis to prevent localized tissue toxicity [106].
- Size Monodispersity: Polydispersity indices (PDI) < 0.1 to maintain consistent cellular uptake resistance and reproducible diffusion kinetics [22, 100].
- Validated Sterility: Cleanroom processing using terminal gamma irradiation or aseptic nanofiltration to guarantee zero microbial contamination [104, 105].

8.2. Medical Data Privacy and Visual Biometric Exposure

Directly displaying biomarker levels on human skin creates distinct bioethical and data privacy concerns [14, 107]. Colorimetric tattoos with visible optical outputs turn an individual's skin into a public diagnostic readout [14, 107]. Observers could infer private medical conditions such as sudden glycemic excursions, systemic lactacidemia, or underlying organ stress without the individual's consent [107, 108]. This visible display risks unwanted medical disclosure, workplace bias, and social stigmatization [107].

Addressing visual exposure risks drives interest toward near-infrared (NIR) or ultraviolet fluorophores that remain completely invisible under normal ambient room light [10, 13, 52]. These formulations keep the diagnostic reading private, requiring dedicated optoelectronic devices or specialized optical filters to capture and decode the signal [10, 52].

Simultaneously, digital telemetry streams between wearable optical patches and cloud systems must incorporate end-to-end cryptographic protocols to protect transmitted patient health metrics under international privacy regulations like HIPAA and GDPR [1, 109].

8.3. *In Vivo* Permanence and Sensor Reversibility

Traditional cosmetic tattooing is permanent; macrophages engulf insoluble ink particles, and dense collagen matrices lock them into the dermis for decades [14, 87]. In contrast, active biosensor inks experience eventual chemical failure through photobleaching, enzymatic deactivation, or matrix degradation [20, 24]. If an injected sensor degrades, an inactive, non-functional formulation remains in the dermal bed [14, 20].

Removing depleted sensor matrices through conventional laser tattoo removal relies on short-pulse Q-switched lasers to mechanically fracture particles via localized photothermal shock [87, 110]. This process breaks components down into fragments small enough for systemic clearance through the lymphatic system [87, 110]. However, applying high-energy laser pulses to functional organic chromophores, quantum dots, or polymer complexes risks generating toxic, mutagenic, or carcinogenic photolytic breakdown products [106, 110].

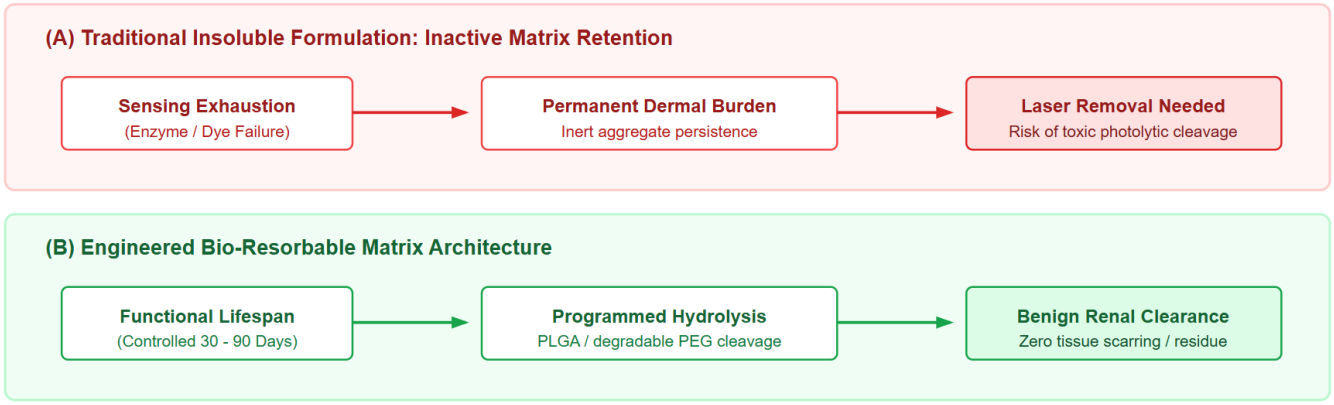

Figure 11. Comparison of Inactive Matrix Retention versus Bio-Resorbable Systems

To establish practical lifecycles, research is turning toward engineered bio-resorbable matrix architectures [25, 111]. Formulations based on crosslinked, hydrolytically degradable polymers such as tailored poly(lactic-co-glycolic acid) (PLGA) or degradable poly(ethylene glycol) (PEG) hydrogels can be programmed to degrade after a defined operational period (e.g., 30 to 90 days) [111, 112]. Hydrolysis cleaves the structural backbone into non-toxic, water-soluble oligomers that clear safely through regular renal filtration, eliminating the need for invasive physical removal [6, 112].

9. Conclusion

Intradermal smart tattoo biosensors serve as non-obstructive devices for continuous physiological monitoring. Interfacing functional optical formulations directly with dermal interstitial fluid provides access to circulating metabolic markers without continuous transcutaneous penetrations, mechanical anchors, or bulky onboard electronic hardware. These platforms track primary metabolites, critical electrolytes, and homeostatic shifts by pairing responsive fluorophores, multi-enzyme cascades, and supramolecular ion-exchange nanoparticles with *ex vivo* optical telemetry platforms. Translating these biosensing materials from experimental models into human diagnostics requires resolving key mass-transport and chemical degradation challenges. The foreign body cascade, chronic macrophage activation, and fibrotic collagen encapsulation impose diffusion barriers that alter temporal sensor fidelity. At the same time, localized oxidative stress, proteolytic enzyme degradation, and fluorophore photobleaching restrict the functional lifespans of current ink chemistries. Addressing these translational bottlenecks will require coordinated advances in functional biomaterials. Integrating non-fouling zwitterionic hydrogels, active pro-angiogenic matrix cues, sacrificial radical scavengers, and inorganic protective nano-shells offers validated pathways to suppress host immune responses and extend sensor lifespans. Developing synthetic, non-enzymatic affinity receptors, such as molecularly imprinted polymers and boronic acid derivatives, will bypass natural protein stability limits. When combined with near-infrared optoelectronic interfaces, dynamic skin-tone normalization algorithms, bio-resorbable polymer backbones, and clear regulatory validation, intradermal biosensors will establish reliable foundations for continuous, non-obstructive metabolic telemetry in personalized medicine.

References

[1] Bandodkar AJ, Wang J. Non-invasive wearable electrochemical sensors: a review. Trends Biotechnol. 2014;32(7):363-371.

[2] Heikenfeld J, Jajack A, Feldman B, Granger SW, Gaitonde S, Begtrup G, Choi BC. Accessing analytes in biofluids for peripheral biochemical monitoring. Nat Biotechnol. 2019;37(4):407-419.

[3] Pickup JC, Hussain F, Evans ND, Rolinski OJ, Birch DJ. Fluorescence-based glucose sensors. Biosens Bioelectron. 2005;20(12):2555-2565.

[4] Makaram P, Owens D, Aceros J. Trends in worldwide research on continuous glucose monitors. J Diabetes Sci Technol. 2014;8(4):819-827.

[5] Wang J. Electrochemical glucose biosensors. Chem Rev. 2008;108(2):814-825.

[6] Kownacka AE, Vegelyte D, Anton N, Vandamme TF. Clinical translation of continuous glucose monitoring platforms: current trends and future prospects. Biosens Bioelectron. 2018;118:218-228.

[7] Heinemann L. Continuous glucose monitoring (CGM) or flash glucose monitoring (FGM)? J Diabetes Sci Technol. 2018;12(4):747-750.

[8] Vaddiraju S, Burgess DJ, Tomazos I, Jain FC, Papadimitrakopoulos F. Technologies for continuous glucose monitoring: current problems and future promises. J Diabetes Sci Technol. 2010;4(6):1540-1562.

[9] Kim J, Campbell AS, de Ávila BEF, Wang J. Wearable biosensors for healthcare monitoring. Nat Biotechnol. 2019;37(4):389-406.

[10] Elsherif M, Hassan MU, Yetisen AK, Butt H. Wearable optical sensors for biomarker analysis in sweat and interstitial fluid. ACS Nano. 2022;16(1):122-141.

[11] Bariya M, Nyein HYY, Javey A. Wearable sweat sensors. Nat Electron. 2018;1(3):160-171.

[12] Ray TR, Choi J, Bandodkar AJ, Krishnan S, Gutruf P, Tian L, Ghaffari R, Rogers JA. Bio-integrated wearable systems: a comprehensive review. Chem Rev. 2019;119(8):5461-5533.

[13] Jiang N, Butt H, Yetisen AK. Dermal tattoo biosensors for real-time biomarker detection. Adv Mater. 2020;32(15):1904617.

[14] Yetisen AK, Moreddu R, Seichepine F, Jiang N, Vega K, Butt H. Dermal biosensors for continuous blood analysis. Angew Chem Int Ed. 2019;58(31):10506-10513.

[15] Bäumler W, Eibler ET, Hohenleutner U, Sens B, Landthaler M. Q-switch laser technology for tattoo removal. Dermatology. 2000;201(4):361-368.

[16] Wiig H, Swartz MA. Interstitial fluid and lymph formation and transport: physiological regulation and roles in pathology. Physiol Rev. 2012;92(3):1005-1060.

[17] Courbet A, Endy D, Renard E, Molina F, Bonnet J. Detection of pathological biomarkers in human clinical samples via amplifying genetic switches and logic gates. Mol Syst Biol. 2015;11(7):818.

[18] Moreddu R, Elsherif M, Adams H, Moschou D, Cordeiro MF, Yetisen AK. Integration of paper sensors into contact lenses and dermal interfaces for tear and interstitial fluid tracking. Lab Chip. 2020;20(21):3970-3979.

[19] Wilson GS, Gifford R. Biosensors for real-time *in vivo* measurements. Biosens Bioelectron. 2005;20(12):2388-2403.

[20] Wisniewski N, Reichert M. Methods for reducing biosensor membrane biofouling. Colloids Surf B Biointerfaces. 2000;18(3-4):197-219.

[21] Anderson JM, Rodriguez A, Chang DT. Foreign body reaction to biomaterials. Semin Immunol. 2008;20(2):86-100.

[22] Sheikh Z, Brooks PJ, Barzilay O, Fine N, Glogauer M. Macrophages, foreign body giant cells, and their response to implantable biomaterials. Materials. 2015;8(9):5671-5701.

[23] Ward WK. A review of the foreign body response to subcutaneously implanted devices: the role of macrophages and fibrovascular tissue. J Diabetes Sci Technol. 2008;2(5):768-777.

[24] Resch-Genger U, Grabolle M, Cavaliere-Jaricot S, Nitschke R, Nann T. Quantum dots versus organic dyes as fluorescent labels. Nat Methods. 2008;5(9):763-775.

[25] Balance WC, Qin EC, Chung HJ, Kong H. Biocompatibility and long-term *in vivo* tracking of intradermal hydrogel biosensors. Biomaterials. 2021;275:120910.

[26] Argyo C, Weiss V, Bräuchle C, Bein T. Multifunctional mesoporous silica nanoparticles as smart nanocarriers. Chem Mater. 2014;26(1):435-451.

[27] Gowers SA, Curto VF, Senosi CA, Rogers ML, Terracciano CM, Boutelle MG, O'Hare D. 3D printed microfluidic sensing platforms for physiological fluid analysis. ACS Sensors. 2019;4(4):983-991.

[28] Kanitakis J. Anatomy, histology and immunohistochemistry of normal human skin. Eur J Dermatol. 2002;12(4):390-401.

[29] Menon GK, Cleary GW, Lane ME. The structure and function of the stratum corneum. Int J Pharm. 2012;435(1):3-9.

[30] Elias PM. Stratum corneum defensive functions: an integrated view. J Invest Dermatol. 2005;125(2):183-200.

[31] Kaushik S, Hord AH, Denson DD, McAllister DV, Smitra S, Allen MG, Prausnitz MR. Lack of pain associated with microfabricated microneedles. Anesth Analg. 2001;92(2):502-504.

[32] Frantz C, Stewart KM, Weaver VM. The extracellular matrix at a glance. J Cell Sci. 2010;123(24):4195-4200.

[33] Peppas NA, Hilt JZ, Khademhosseini A, Langer R. Hydrogels in biology and medicine: from molecular principles to bionanotechnology. Adv Mater. 2006;18(11):1345-1360.

[34] Braverman IM. The cutaneous microcirculation. J Investig Dermatol Symp Proc. 2000;5(1):3-9.

[35] Johnson PC. Autoregulation of blood flow. Circ Res. 1986;59(5):483-495.

[36] Levick JR, Michel CC. Microvascular fluid exchange and the revised Starling principle. Cardiovasc Res. 2010;87(2):198-210.

[37] Scallan J, Huxley VH, Korthuis RJ. Capillary fluid exchange: regulation, functions, and pathology. Colloq Ser Integr Syst Physiol From Mol to Funct. 2010;2(1):1-94.

[38] Swartz MA. The physiology of the lymphatic system. Adv Drug Deliv Rev. 2001;50(1-2):3-20.

[39] Crank J. The Mathematics of Diffusion. 2nd ed. Oxford: Oxford University Press; 1979.

[40] Basu A, Dube S, Slama M, Errazuriz I, Amezcua JC, Kudva YC, Peyser T, Carter RE, Cobelli C, Basu R. Time lag of glucose from intravascular to interstitial compartment in humans. Diabetes. 2013;62(12):4083-4087.

[41] Bankar SB, Bule MV, Singhal RS, Ananthanarayan L. Glucose oxidase an overview. Biotechnol Adv. 2009;27(4):489-501.

[42] Rassaei L, Olthuis W, Tsujimura S, van den Berg A. Lactate biosensors: current status and outlook. Anal Bioanal Chem. 2014;406(1):123-137.

[43] Gooding JJ. Electrochemical enzyme biosensors: synthesis and applications. Electroanalysis. 2006;18(1):15-28.

[44] Josephy PD, Eling T, Mason RP. The horseradish peroxidase-catalyzed oxidation of 3,3',5,5'-tetramethylbenzidine. J Biol Chem. 1982;257(7):3669-3675.

[45] Bakker E, Bühlmann P, Pretsch E. Carrier-based ion-selective electrodes and bulk optodes. 1. General characteristics. Chem Rev. 1997;97(8):3083-3132.

[46] Xie X, Bakker E. Ion selective optodes: from the macroscopic to the nanoscale. Anal Bioanal Chem. 2015;407(14):3899-3910.

[47] Spichiger UE. Chemical Sensors and Biosensors for Medical and Biological Applications. Weinheim: Wiley-VCH; 1998.

[48] Shortreed M, Bakker E, Kopelman R. Miniature sodium-selective ion-exchange optode with fluorescent readout. Anal Chem. 1996;68(15):2656-2662.

[49] Weissleder R. A clearer vision for *in vivo* imaging. Nat Biotechnol. 2001;19(4):316-317.

[50] Anderson RR, Parrish JA. The optics of human skin. J Invest Dermatol. 1981;77(1):13-19.

[51] Jacques SL. Optical properties of biological tissues: a review. Phys Med Biol. 2013;58(11):R37-R61.

[52] Hong G, Antaris AL, Dai H. Near-infrared fluorophores for biomedical imaging. Nat Biomed Eng. 2017;1(1):0010.

[53] Smith AM, Mancini MC, Nie S. Second window for *in vivo* imaging. Nat Nanotechnol. 2009;4(11):710-711.

[54] de Silva AP, Gunaratne HQ, Gunnlaugsson T, Huxley AJ, McCoy CP, Rademacher JT, Rice TE. Signaling recognition events with fluorescent sensing constructs. Chem Rev. 1997;97(5):1515-1566.

[55] Valeur B, Leray I. Design principles of fluorescent molecular sensors for cation recognition. Coord Chem Rev. 2000;205(1):3-40.

[56] Jares-Erijman EA, Jovin TM. FRET imaging. Nat Biotechnol. 2003;21(11):1387-1395.

[57] Medintz IL, Clapp AR, Mattoussi H, Goldman ER, Fisher B, Mauro JM. Self-assembled nanoscale biosensors based on quantum dot FRET donors. Nat Mater. 2003;2(9):630-638.

[58] Barone PW, Baik S, Heller DA, Strano MS. Near-infrared optical sensors based on single-walled carbon nanotubes. Nat Mater. 2005;4(1):86-92.

[59] Michalet X, Pinaud FF, Bentolila LA, Tsay JM, Doose S, Li JJ, Sundaresan G, Wu AM, Weiss S. Quantum dots for live cells, *in vivo* imaging, and diagnostics. Science. 2005;307(5709):538-544.

[60] Liu X, Tang TC, Tham E, Yuk H, Lin S, Lu TK, Zhao X. Stretchable living materials and devices with hydrogel-elastomer hybrids. Proc Natl Acad Sci USA. 2017;114(9):2200-2205.

[61] Slomovic S, Pardee K, Collins JJ. Synthetic biology devices for *in vitro* and *in vivo* diagnostics. Proc Natl Acad Sci USA. 2015;112(47):14429-14435.

[62] Tsien RY. The green fluorescent protein. Annu Rev Biochem. 1998;67(1):509-544.

[63] Inda ME, Broset E, Lu TK, de la Fuente-Nunez C. Emerging applications of synthetic biology in dermatology. J Invest Dermatol. 2019;139(10):2083-2090.

[64] Gerber FX, Fussenegger M. Synthetic biology-based therapeutic gene circuits for metabolic disorders. Curr Opin Chem Biol. 2020;58:26-34.

[65] American Diabetes Association. Standards of Care in Diabetes 2024. Diabetes Care. 2024;47(Suppl 1):S1-S343.

[66] Sode K, Tsugawa W, Ferri S, Asano R. Engineering of glucose sensing enzymes for continuous glucose monitoring. J Diabetes Sci Technol. 2016;10(6):1228-1234.

[67] James TD, Sandanayake KRAS, Shinkai S. Saccharide sensing with molecular receptors based on boronic acid. Nature. 1995;374(6520):345-347.

[68] Springsteen G, Wang B. A detailed examination of boronic acid-diol complexation. Tetrahedron. 2002;58(26):5291-5300.

[69] Sun X, James TD, Anslyn EV. Synthetic receptors for carbohydrate recognition. Chem Soc Rev. 2018;47(6):2289-2317.

[70] Bakker J, Nijsten MW, Jansen TC. Clinical use of lactate monitoring in critically ill patients. Ann Intensive Care. 2013;3(1):12.

[71] Garjonyte R, Melvydas V, Malinauskas A. Lactate biosensors based on immobilized lactate oxidase. Sens Actuators B Chem. 2006;116(1-2):129-134.

[72] Schreml S, Meier RJ, Wolfbeis OS, Landthaler M, Szeimies RM, Babilas P. 2D luminescence imaging of pH *in vivo*. Proc Natl Acad Sci USA. 2011;108(6):2432-2437.

[73] Steinegger A, Wolfbeis OS, Borisov SM. Optical sensing and imaging of pH values: methodologies, sensors, and applications. Chem Rev. 2020;120(22):12357-12489.

[74] Rock KL, Kataoka H, Lai JJ. Uric acid as a danger signal in health and disease. Nat Rev Rheumatol. 2013;9(1):13-23.

[75] Erden PE, Kılıç E. A review of enzymatic uric acid biosensors based on various nanomaterials. Talanta. 2013;107:312-323.

[76] Sellergren B. Molecularly imprinted polymers: man-made mimics of antibodies and their applications in analytical chemistry. TrAC Trends Anal Chem. 2000;16(6):310-320.

[77] Doumas BT, Watson WA, Biggs HG. Albumin standards and the measurement of serum albumin with bromcresol green. Clin Chim Acta. 1971;31(1):87-96.

[78] Wilson CJ, Clegg RE, Leavesley DI, Pearcy MJ. Mediation of biomaterial-cell interactions by adsorbed proteins: a review. Tissue Eng. 2005;11(1-2):1-18.

[79] Nathan C. Neutrophils and immunity: challenges and opportunities. Nat Rev Immunol. 2006;6(3):173-182.

[80] Babior BM. Phagocytes and oxidative stress. Am J Med. 2000;109(1):33-44.

[81] McNally AK, Anderson JM. Macrophage fusion and multinucleated giant cells of native and foreign body origin. Transplantation. 2011;91(12):1285-1290.

[82] Wynn TA, Ramalingam TR. Mechanisms of fibrosis: translation to therapeutic targets. Nat Med. 2012;18(7):1028-1040.

[83] Hinz B, Phan SH, Thannickal VJ, Galli A, Bochaton-Piallat ML, Gabbiani G. The myofibroblast: one function, multiple origins. Am J Pathol. 2007;170(6):1807-1816.

[84] Sharkawy AA, Klitzman B, Truskey GA, Reichert WM. Engineering the tissue-sensor interface: assessing the foreign body response and its effect on transport. J Biomed Mater Res. 1997;37(3):401-412.

[85] Danielsson B, Mosbach K. Enzyme stabilization for biosensor deployment. FEBS Lett. 1987;212(2):233-238.

[86] Eggeling C, Widengren J, Rigler R, Seidel CA. Photobleaching of fluorescent dyes investigated by single-molecule spectroscopy. Anal Chem. 1998;70(13):2651-2659.

[87] Schreiver I, Hesse B, Seim C, Castillo-Michel H, Villanova J, Laux P, Dreiack N, Penning R, Tucoulou R, Cotte M, Luch A. Synchrotron-based tracking of tattoo pigment migration from skin to lymph nodes. Sci Rep. 2017;7(1):11395.

[88] Laux P, Tralau T, Tentschert J, Blume A, Dahms S, Bäumler W, Bernstein E, Bocca B, Alimonti A, Colebrook H, Luch A. A medical-toxicological view of tattooing. Lancet. 2016;387(10016):395-402.

[89] Jiang S, Cao Z. Ultralow-fouling, zwitterionic polymers. Adv Mater. 2010;22(9):920-932.

[90] Chen S, Zheng J, Li L, Jiang S. Strong resistance of phosphorylcholine self-assembled monolayers to protein adsorption. J Am Chem Soc. 2005;127(41):14473-14478.

[91] Schlenoff JB. Zwitteration: the new antiscaling. Langmuir. 2014;30(32):9625-9636.

[92] Ferrara N, Davis-Smyth T. The biology of vascular endothelial growth factor. Endocr Rev. 1997;18(1):4-25.

[93] Norton LW, Koschwanez HE, Wisniewski NA, Klitzman B, Reichert WM. Vascular endothelial growth factor incorporated into biosensors promotes local angiogenesis. J Biomed Mater Res A. 2007;81(4):858-869.

[94] Chance B, Greenstein DS, Roughton FJ. The mechanism of catalase action. Arch Biochem Biophys. 1952;37(2):301-339.

[95] Updike SJ, Hicks GP. The enzyme electrode. Nature. 1967;214(5092):986-988.

[96] Kresge CT, Leonowicz ME, Roth WJ, Vartuli JC, Beck JS. Ordered mesoporous molecular sieves synthesized by a liquid-crystal template mechanism. Nature. 1992;359(6397):710-712.

[97] Vallet-Regí M, Balas F, Arcos D. Mesoporous materials for drug delivery. Angew Chem Int Ed. 2007;46(40):7548-7558.

[98] Ow H, Larson DR, Srivastava M, Baird BA, Webb WW, Wiesner U. Bright and stable core-shell fluorescent silica nanoparticles. Nano Lett. 2005;5(1):113-117.

[99] Peppas NA, Merrill EW. Crosslinked poly(vinyl alcohol) hydrogels as swollen elastic networks. J Appl Polym Sci. 1977;21(7):1763-1770.

[100] Xie X, Zhai J, Bakker E. Potentiometric and optical sensors based on nanospheres. Anal Chem. 2014;86(6):2853-2865.

[101] Shen L, Hagen JA, Papautsky I. Point-of-care colorimetric detection using a smartphone. Lab Chip. 2012;12(21):4240-4243.

[102] Kollias N, Baqer A. Spectrophotometric evaluation of melanin pigmentation in human skin. Photochem Photobiol. 1985;42(3):297-301.

[103] Kim J, Gutruf P, Chiarelli AM, Heo SY, Cho KW, Xie Z, Talarico D, Ma Y, Jang JW, Liu Z, Rogers JA. Miniaturized flexible electronic systems for wireless optical sensing of tissue hemodynamics. Adv Funct Mater. 2017;27(1):1604373.

[104] US Food and Drug Administration. General Considerations for Clinical Studies of Medical Devices: Guidance for Industry and Food and Drug Administration Staff. Silver Spring: US Department of Health and Human Services; 2020.

[105] International Organization for Standardization. Biological evaluation of medical devices Part 1: Evaluation and testing within a risk management process. ISO Standard No. 10993-1:2018. Geneva: ISO; 2018.

[106] Manso PRM, Papoila AL. Analytical composition of tattoo inks: heavy metals and organic impurities. Contact Dermatitis. 2019;80(6):345-353.

[107] Viseu A. Biosensors and the quantified self: personal health tracking and public visibility. Sci Technol Human Values. 2015;40(3):342-365.

[108] Lupton D. The quantified self: an introduction to digital health sociology. Digit Health. 2014;1(1):1-15.

[109] Gostin LO, Halabi SF. The regulatory paradigm for digital health platforms under HIPAA and GDPR. JAMA. 2018;320(3):233-234.

[110] Vasold R, Naarmann N, Ulrich H, Fischer D, König B, Landthaler M, Bäumler W. Tattoo pigments are cleaved by laser light into dangerous photoproducts. Photochem Photobiol. 2004;80(2):185-190.

[111] Danhier F, Ansorena E, Silva JM, Coco R, Le Breton A, Préat V. PLGA-based nanoparticles: an overview of biomedical applications. J Control Release. 2012;161(2):505-522.

[112] Place ES, George JH, McKay CK, Stevens MM. Synthetic polymer scaffolds for regenerative engineering. Nat Mater. 2009;8(6):457-470.